Chinese Chemical Letters 36 (2025) 110429

Contents lists available at ScienceDirect

Chinese Chemical Letters

journal homepage: www.elsevier.com/locate/cclet

N-doped carbon confined ternary Pt_2NiCo intermetallics for efficient oxygen reduction reaction

Chenhao Zhang[a,b], Qian Zhang[a], Yezhou Hu[c], Hanyu Hu[a], Junhao Yang[a], Chang Yang[a], Ye Zhu[c], Zhengkai Tu[d], Deli Wang[a,b,*]

[a] Key Laboratory of Material Chemistry for Energy Conversion and Storage, Hubei Key Laboratory of Material Chemistry and Service Failure, School of Chemistry and Chemical Engineering, Huazhong University of Science and Technology, Wuhan 430074, China
[b] China-EU Institute for Clean and Renewable Energy, Huazhong University of Science and Technology, Wuhan 430074, China
[c] Department of Applied Physics, The Hong Kong Polytechnic University, Hong Kong 999077, China
[d] School of Energy and Power Engineering, Huazhong University of Science and Technology, Wuhan 430074, China

ARTICLE INFO

Article history:
Received 3 June 2024
Revised 4 September 2024
Accepted 6 September 2024
Available online 7 September 2024

Keywords:
Oxygen reduction reaction
Electrocatalysis
Ordered intermetallic
Toxicity tolerance
Carbon confinement

ABSTRACT

Developing high performance electrocatalysts for the cathodic oxygen reduction reaction (ORR) is essential for the widespread application of fuel cells. Herein, a promising Pt_2NiCo atomic ordered ternary intermetallic compound with N-doped carbon layer coating (*o*-Pt_2NiCo@NC) has been synthesized *via* a facile method and applied in acidic ORR. The confinement effect provided by the carbon layer not only inhibits the agglomeration and sintering of intermetallic nanoparticles during high temperature process but also provides adequate protection for the nanoparticles, mitigating the aggregation, detachment and poisoning of nanoparticles during the electrochemical process. As a result, the *o*-Pt_2NiCo@NC demonstrates a mass activity (MA) and specific activity (SA) of 0.65 A/mg_{Pt} and 1.41 mA/cm_{Pt}^2 in 0.1 mol/L $HClO_4$, respectively. In addition, after 30,000 potential cycles from 0.6 V to 1.0 V, the MA of *o*-Pt_2NiCo@NC shows much lower decrease than the disordered Pt_2NiCo alloy and Pt/C. Even cycling at high potential cycles of 1.5 V for 10,000 cycles, the MA still retains ~70%, demonstrating superior long-term durability. Furthermore, the *o*-Pt_2NiCo@NC also exhibits strong tolerance to CO, SO_x, and PO_x molecules in toxicity tolerance tests. The strategy in this work provides a novel insight for the development of ORR catalysts with high catalytic activity, durability and toxicity tolerance.

The depletion of fossil fuel and the subsequent environmental pollution problems have sparked a significant surge in demand for clean and renewable energy sources [1–3]. Proton exchange membrane fuel cells (PEMFCs) have garnered considerable attention in the realm of energy conversion and storage technologies due to their distinct advantages, including high energy density, environmental friendliness, and liberation from the constraints of the Carnot cycle [4–6]. However, the sluggish kinetics of the oxygen reduction reaction (ORR) in the cathode of the PEMFCs greatly impede the overall efficiency and hinder its commercial viability [7–10]. Consequently, the development of high-performance ORR catalysts is of paramount importance [11]. Currently, Pt-based catalysts have been extensively investigated for their optimal oxygen reduction properties, but the limited reserves and exorbitant cost of Pt pose a challenge [12–14]. To tackle this issue, various optimization strategies for Pt-based ORR catalysts have been proposed. One efficient strategy involves alloying Pt with transition metal (M), the introduction of M can modulate the d-band center and electronic structure of Pt, thus optimizing its adsorption capability for oxygen-contained intermediates during ORR process, which can effectively enhance the catalyst's activity while reducing the amount of Pt [15–17]. Unfortunately, transition metals in conventional disordered alloys are prone to dissolution and corrosion in acidic electrolyte during prolonged operation of the PEMFCs. resulting in poor long-term durability and lifespan [18]. In contrast, ordered intermetallic compounds (IMC) exhibit superior durability due to their highly controllable structure, stronger Pt-M metallic bonding, and robust coupling between the 3d-5d orbitals of the transition metal and Pt [19,20], which has received much attention as a new class of catalysts. In recent years, a notable volume of investigation has been dedicated to binary Pt-M intermetallic compound systems for catalytic ORR such as Pt-Co [21,22], Pt-Fe [23,24], Pt-Cu [25], Pt-Zn [26], Pt-Pb [27]. Recently, ternary intermetallic compounds Pt-M_1–M_2 have also gradually attracted much attention from researchers.

* Corresponding author.
E-mail address: wangdl81125@hust.edu.cn (D. Wang).

https://doi.org/10.1016/j.cclet.2024.110429
1001-8417/

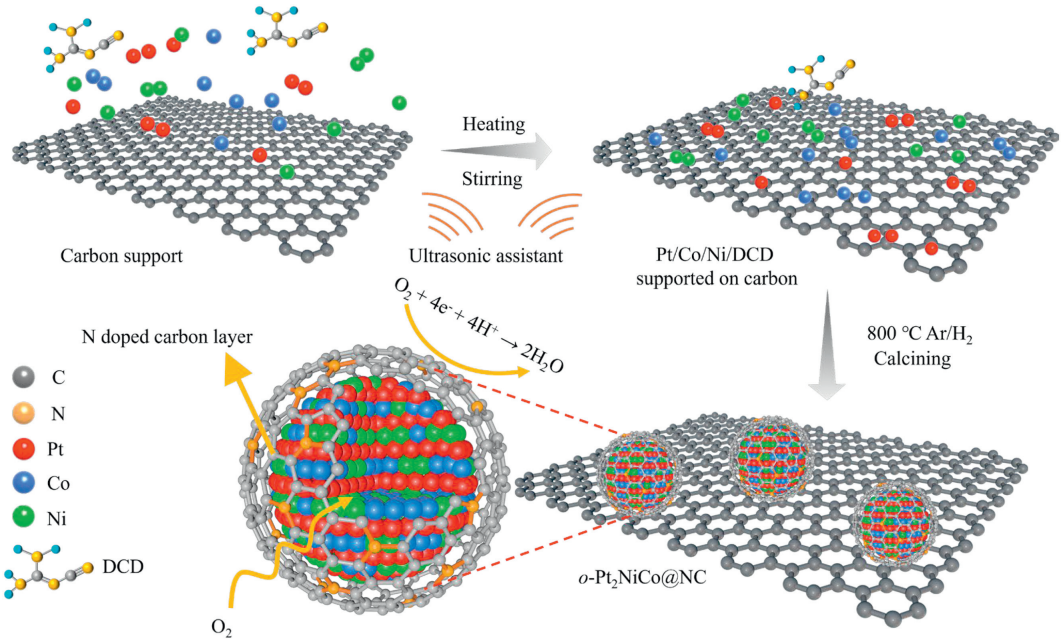

Fig. 1. Schematic diagram of the preparation of *o*-Pt_2NiCo@NC.

The introduction of a third metal allows for further manipulation of the electronic structure of Pt. Additionally, the synergistic effect between M_1 and M_2 has shown potential in enhancing the ORR activity and durability [28]. However, high temperature annealing is an essential step in the preparation of the vast majority of Pt-based IMC. This process leads to an excessive increase in catalyst particle size due to the particle sintering, resulting in insufficient exposure of active sites on the catalyst surface [29]. Furthermore, during the actual operation of the PEMFCs, some toxic molecules will inevitably be mixed in the reaction gas. Once these toxic molecules come into contact with the catalyst, they will firmly adsorb on the surface of the Pt active sites, poisoning the catalyst, which severely affects the stable operation of fuel cells [30]. Therefore, the development of ternary Pt-based IMC as electrocatalysts for oxygen reduction reaction with relatively small particles and superior activity, durability and toxicity tolerance still remains a challenging task.

In recent research on Pt-based ORR catalysts, the confinement strategy has garnered increasing attention from researchers due to its unique advantages [31]. The core idea of the confinement strategy is to confine the catalyst to a specific space consisting of confinement layers and carriers. The presence of a confining layer can effectively restrict the particle growth and agglomeration during high temperature process and protect them from agglomeration and shedding during the working process. Meanwhile, Among the many types of coating layers, carbon layers have attracted much attention due to their inexpensive precursor carbon source, superior electrical conductivity, abundant pore structures, and simple design and preparation steps. Nevertheless, confinement strategy has been rarely studied and applied in Pt-based ternary intermetallic systems.

Herein, we report a ternary Pt_2NiCo IMC of N-doped carbon layer confinement (denoted as *o*-Pt_2NiCo@NC). The N-doped carbon layer confinement can not only effectively inhibit the agglomeration and sintering of Pt_2NiCo nanoparticles in the formation of the ordered structure by high-temperature annealing process, but also mitigate particle agglomeration, detachment and poisoning during fuel cell practical operation conditions. More importantly, the electrochemical test results demonstrate that *o*-Pt_2NiCo@NC exhibits superior ORR activity, the mass activity (MA) at 0.9 V of *o*-Pt_2NiCo@NC is 2.6 and 4.1 times higher than that of carbon supported disordered Pt_2NiCo alloy and Pt/C, respectively. After 30,000 potential cycles from 0.6 V to 1.0 V and 10,000 high potential cycles from 1.0 V to 1.5 V, the MA of *o*-Pt_2NiCo@NC still retains 80.2% and 69.1%. Additionally, the *o*-Pt_2NiCo@NC also exhibits enhanced tolerance toward CO, SO_x and PO_x due to the protection provided by the N-doped carbon layer.

The *o*-Pt_2NiCo@NC was synthesized by a facile impregnation-reduction method (see Supporting information for experimental details), and the process is shown in Fig. 1. Firstly, dicyandiamide (DCD) as a nitrogen and carbon source were uniformly dispersed on the surface of the carbon support through the impregnation process together with the metal salt precursor. Subsequently, in a one-step high-temperature pyrolytic reduction process, DCD is first converted to graphitic carbon nitride (g-C_3N_4) at about 550 °C and further decomposed into N-doped carbon layers and encapsulated on the Pt_2NiCo nanoparticles at nearly 800 °C [32,33]. Meanwhile, the metal ions in the precursors are also reduced and transformed from disordered alloys to ordered Pt_2NiCo IMC prompted by high temperature Ar/H_2 atmosphere. The disordered carbon supported Pt_2NiCo alloy nanoparticles and Pt/C are chosen as comparison samples, the loading of each metal element in the three catalysts was measured by inductively coupled plasma-optical emission spectroscopy (ICP-OES), which are shown in Table S1 (Supporting information). The results indicate that the loading of Pt in *o*-Pt_2NiCo@NC is 17.8%, slightly lower than 20%, which may be attributed to the introduction of DCD.

X-ray diffraction (XRD) was employed to determine the crystalline structure of *o*-Pt_2NiCo@NC. The XRD patterns of *o*-Pt_2NiCo@NC and the comparison samples (Fig. 2a) all reveal three diffraction peaks at approximately 39°, 46°, and 67° These peaks correspond to the (111), (200), and (220) facets of Pt, as indicated by the Pt PDF standard card. Notably, both *o*-Pt_2NiCo@NC and *d*-Pt_2NiCo exhibit an obvious rightward shift in the diffraction peak positions compared with Pt/C. This rightward shift indicates that the introduction of Ni and Co atoms with smaller diameters will cause the lattice contraction of Pt [34,35]. Additionally, *o*-Pt_2NiCo@NC displays extra superlattice diffraction peaks at 23.8°, 33.7°, and 49.1°, which correspond to the (001), (110), and (002) intermetallic facets. These peaks align with the standard PDF

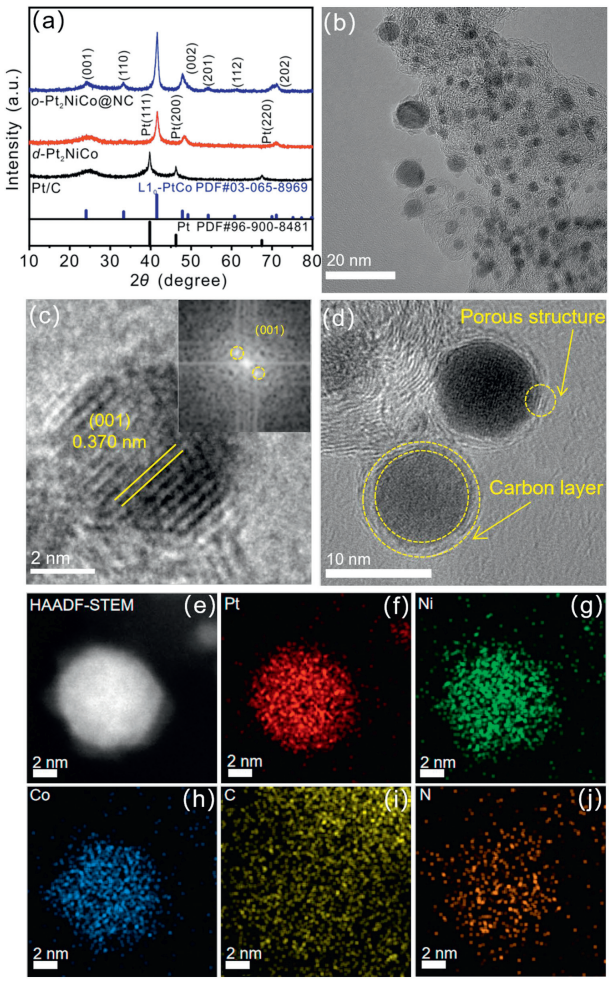

Fig. 2. (a) XRD patterns of *o*-Pt_2NiCo@NC, *d*-Pt_2NiCo and Pt/C. The blue vertical line corresponds to $L1_0$-type intermetallic PtCo (PDF card No. 03–065–8969) and the black vertical lines correspond to Pt (PDF card No. 96–900–8481). (b) The low-magnification TEM image of *o*-Pt_2NiCo@NC. (c, d) HR-TEM images of *o*-Pt_2NiCo@NC and the corresponding FFT pattern. (e-j) HAADF-STEM and corresponding elemental mapping of Pt, Ni, Co, C, N.

cards of $L1_0$-PtCo, confirming the presence of an $L1_0$-type ordered structure in *o*-Pt_2NiCo@NC.

Transmission electron microscopy (TEM) was performed to analyze the microstructure of the catalyst. The low magnification TEM image of *o*-Pt_2NiCo@NC (Fig. 2b) illustrated that the catalyst nanoparticles are uniformly dispersed on the carbon support with an average particle size of only 3.32 nm (Fig. S1 in Supporting information). The particle size of *o*-Pt_2NiCo@NC has a significant reduction compared with the catalyst synthesized by the same method without the addition of DCD (Fig. S2 in Supporting information). This indicates that the carbon layer confinement can effectively inhibit the particle sintering and agglomeration during the high-temperature ordering process of the Pt_2NiCo particles. Fig. 2c demonstrates the HR-TEM images of *o*-Pt_2NiCo@NC, in which the lattice stripe with a spacing of 0.370 nm corresponds to the superlattice (001) of the Pt_2NiCo intermetallic compound. The corresponding FFT images of *o*-Pt_2NiCo@NC also exhibit diffraction spots of the (001) superlattice, confirming the formation of the ordered intermetallic compound structure. In the HR-TEM pattern of Fig. 2d, it can be observed that the Pt_2NiCo nanoparticles are encapsulated in a carbon layer with a thickness of about 1.0 nm. The presence of pore structure can also be observed on the carbon layer, which can be attributed to the diffusion of CN_x gas produced by the decomposition of g-C_3N_4 from DCD during the high temperature treatment process. Figs. 2e-j illustrates the HAADF-STEM and corresponding elemental mapping of single *o*-Pt_2NiCo@NC nanoparticles, the metal elements Pt, Ni, and Co are uniformly dispersed in the nanoparticles without any obvious segregation on the surface or enrichment in the interior. Meanwhile, the presence of N element can also be clearly observed, which indicates the N element doping into the carbon layer successfully.

X-ray photoelectron spectroscopy (XPS) was performed to analyze the valence distribution of elements on the surface of *o*-Pt_2NiCo@NC. Fig. S3 (Supporting information) illustrates the XPS survey spectrum of *o*-Pt_2NiCo@NC and *d*-Pt_2NiCo, in which there is an obvious N 1s signal peak at around 400.0 eV binding energy for *o*-Pt_2NiCo@NC, while no signal peak is observed at the same position for *d*-Pt_2NiCo, which initially indicates the introduction of N elements in *o*-Pt_2NiCo@NC. Fig. S4a (Supporting information) shows the C 1s high resolution XPS spectrum of *o*-Pt_2NiCo@NC. It could be deconvolved into four signal peaks located at 284.8 eV, 285.1 eV, 286.0 eV, and 288.9 eV, which correspond to C–C, C–N, C–O, and C = O bonds, respectively, in which the presence of the C–N bond further confirms that the N element is successfully doped into the carbon layer [36]. To investigate the role of N element doping into the carbon layer in *o*-Pt_2NiCo@NC, the N 1s high resolution XPS spectrum was also deconvoluted. As shown in Fig. S2b (Supporting information), there are three signal peaks at binding energies of 399.1 eV, 401.1 eV and 404.2 eV, corresponding to pyridinic nitrogen, graphitic nitrogen and nitrogen oxide, respectively [37]. The pyridinic nitrogen can provide ORR active sites and modify the electronic structure of the catalyst, while the graphitic nitrogen can enhance the conductivity of the carbon layer and thus accelerating the electron transfer rate, both of which contribute to the improvement of the ORR performance of the catalyst [38,39]. The Pt 4f high resolution XPS spectrum of *o*-Pt_2NiCo@NC and *d*-Pt_2NiCo (Fig. S5 in Supporting information) can be deconvoluted into two pairs of peaks. The peaks located at 71.8 eV, 75.4 eV and the peaks located at 72.4 eV, 76.0 eV can be assigned to metallic Pt^0 and oxidation state Pt^{2+}, respectively [18]. Notably, the binding energy of the peak Pt $4f_{7/2}$ of *o*-Pt_2NiCo@NC is shifted right by 0.3 eV compared with that of *d*-Pt_2NiCo, which indicates that the N-doped carbon layer and internal ordering structure of Pt_2NiCo can optimize the electronic structure of Pt, weaken its adsorption strength to ORR oxygen-contained intermediates to a more moderate level, thus enhance its ORR performance [40,41]. The Ni and Co 2p high resolution XPS spectrum of *o*-Pt_2NiCo@NC are shown in Fig. S6 (Supporting information), where the Ni 2p spectrum can be decomposed into three pairs of peaks corresponding to Ni^0 (852.9 eV *vs.* 870.1 eV), Ni^{2+} (855.4 eV *vs.* 872.6 eV), and the satellite peaks of Ni (861. 4 eV *vs.* 878.8 eV), respectively [42]. Similarly, the Co 2p spectrum can also be decomposed into three pairs of peaks corresponding to Co^0 (778.5 eV *vs.* 793.5 eV), Co^{2+} (780.7 eV *vs.* 796.7 eV) and the satellite peaks of Co (784.8 eV *vs.* 802.8 eV), respectively [43]. Based on the XPS analysis results, it can be seen that the Pt on the surface of *o*-Pt_2NiCo@NC exists mainly in the metallic state, while the Ni and Co exist mainly in the oxidized state, which is consistent with the valence distribution previously reported in the literature regarding the formation of IMC between Pt and M [44].

The Raman spectra of *o*-Pt_2NiCo@NC, *d*-Pt_2NiCo and Vulcan XC-72 carbon support are illustrated in Fig. S7 (Supporting information), all the samples exist two signal peaks located at 1350 cm^{-1} and 1590 cm^{-1}, which correspond to the D-band and the G-band of the carbon materials, respectively. The ratio of the peak intensities of the D-band to the G-band (I_D/I_G) can reflect the degree of the defects in the graphite structure [45,46]. The I_D/I_G value of *o*-Pt_2NiCo@NC (1.15) is higher than that of *d*-Pt_2NiCo (1.08) and both are higher than that of Vulcan XC-72 (1.01), which sug-

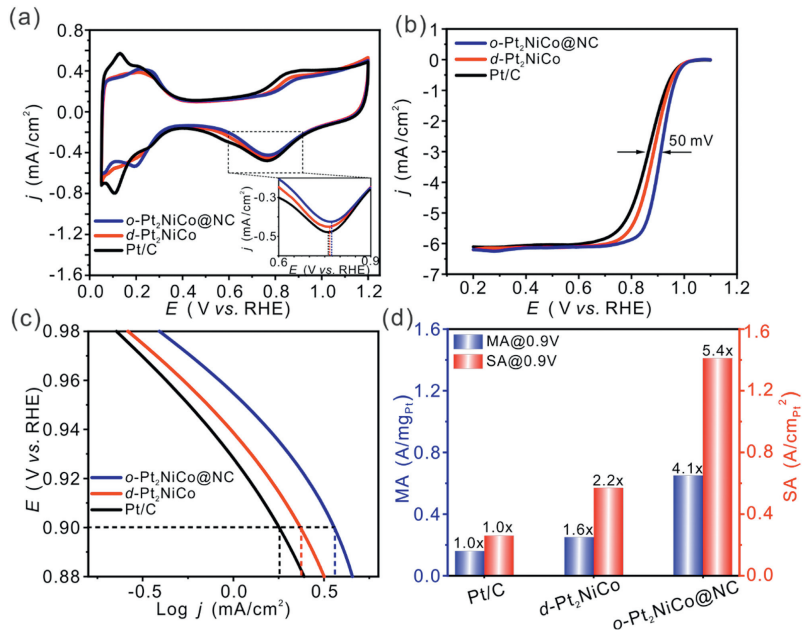

Fig. 3. (a) CV curves of *o*-Pt_2NiCo@NC, *d*-Pt_2NiCo and Pt/C in N_2-saturated 0.1 mol/L $HClO_4$. (b) LSV curves of *o*-Pt_2NiCo@NC, *d*-Pt_2NiCo and Pt/C in O_2-saturated 0.1 mol/L $HClO_4$. (c) Tafel spot and (d) MA and SA of *o*-Pt_2NiCo@NC, *d*-Pt_2NiCo and Pt/C.

gests that the introduction of the N-doped carbon layer with intermetallic nanoparticle loading can create more defects on the surface of the carbon carrier, which contributes to the enhancement of ORR performance [47]. Meanwhile, the specific surface area of *o*-Pt_2NiCo@NC was measured using N_2 adsorption-desorption isotherms (Fig. S8a in Supporting information). The Brunauer–Emmett–Teller (BET) specific surface area of *o*-Pt_2NiCo@NC was 226.6 m^2/g, which was larger than *d*-Pt_2NiCo (159.3 m^2/g), its increased specific surface area could be attributed to the structure of porous carbon layers formed on the surface of *o*-Pt_2NiCo@NC. The pore size distribution curves of the catalysts (Fig. S8b in Supporting information) show that most of the catalysts have a pore size distribution between 2 nm and 10 nm, dominated by mesoporous structures, with the vast majority of the pore sizes larger than the kinetic diameter of O_2 diffusion (0.346 nm) [48]. This indicates that the carbon layer will not affect the O_2 transport during the reaction process. Meanwhile, the large specific surface area of *o*-Pt_2NiCo@NC with abundant mesoporous structure can expose more active sites on the catalyst surface and contribute to the electrolyte transport during the reaction process to further enhance the ORR reaction rate [49,50].

The ORR performance of *o*-Pt_2NiCo@NC was assessed using electrochemical tests. Fig. 3a shows the cyclic voltametric (CV) curves of the three catalysts. The electrochemical active specific area (ECSA) was calculated using the low-potential H_{upd} deposition method [28]. The ECSA of *o*-Pt_2NiCo@NC and *d*-Pt_2NiCo are 46.4 m^2/g and 43.7 m^2/g, respectively, which are smaller than that of Pt/C (60.8 m^2/g) due to particle agglomeration during high-temperature annealing. A larger catalyst particle size will result in insufficient exposure of active sites on their surface. Notably, *o*-Pt_2NiCo@NC annealed at 800 °C exhibited a similar ECSA compared with *d*-Pt_2NiCo which annealed at 500 °C, indicating that the N-doped carbon layer effectively prevented Pt_2NiCo nanoparticles from agglomerating during ordered high-temperature annealing. Furthermore, a slight cathodic oxygen reduction peak shifting to a higher potential of *o*-Pt_2NiCo@NC was observed at approximately 0.8 V (*vs.* RHE). This suggests that the introduction of the N-doped carbon layer and the formation of the ordered structure can optimize the electronic structure of Pt, weaken the adsorption strength between Pt and oxygen-containing intermediates, and enhance the efficiency of the catalysts for oxygen reduction, correspond well with the XPS results. The linear scanning voltametric (LSV) curves of the three catalysts are presented in Fig. 3b. *o*-Pt_2NiCo@NC exhibits the highest half-wave potential (0.913 V), which is significantly superior to *d*-Pt_2NiCo (0.882 V) and Pt/C (0.863 V), which indicates that the *o*-Pt_2NiCo@NC possesses the most remarkable ORR kinetics with the lowest reaction overpotential. Furthermore, the *o*-Pt_2NiCo@NC also exhibits the lowest Tafel slope (Fig. 3c) among the three catalysts, indicating the considerably enhanced ORR kinetic activity [51]. Additionally, Fig. 3d illustrates the calculated MA and specific activity (SA) of these three catalysts at 0.9 V (*vs.* RHE) potentials. *o*-Pt_2NiCo@NC catalyst achieves a MA of 0.65 A/mg_{Pt} and a SA of 1.41 A/cm_{Pt}^2, which are 4.1 and 5.4 times higher than that of Pt/C, 2.6 and 2.5 times higher than that of *d*-Pt_2NiCo, respectively. The ORR electron transfer number of the catalyst is another important indicator of the catalyst quality. According to the relevant literature, N-doped carbon materials have been proven to be effective two-electron ORR catalysts [52].

To investigate whether the introduction of the N-doped carbon layer promotes the two-electron ORR process, the LSV curves of the catalysts at different RDE rotating speeds were measured and the reaction electron transfer number of *o*-Pt_2NiCo@NC was calculated using the K-L equation (Fig. S9 in Supporting information) [2], and the calculated electron transfer number of *o*-Pt_2NiCo@NC and the comparison catalysts were close to 4, which indicated that they followed the direct four-electron ORR pathway, and also indicated that the introduction of the N-doped carbon layer and ordering intermetallic structure did not have an impact on the reaction pathway of the catalysts [53].

Furthermore, the thickness of the carbon layer is also an important factor which can directly affecting the ORR performance of *o*-Pt_2NiCo@NC. The flexible regulation of the carbon layer thickness can be achieved by adjusting the additional amount of DCD in the precursor [54]. Fig. S10a (Supporting information) shows the CV curves of *o*-Pt_2NiCo@NC with different amounts of DCD added in the precursor. When the amount of DCD was increased from 0.3 mmol to 0.6 mmol, the ECSA of the catalyst showed an increase, at this time, the thicker carbon layer could effectively inhibit the

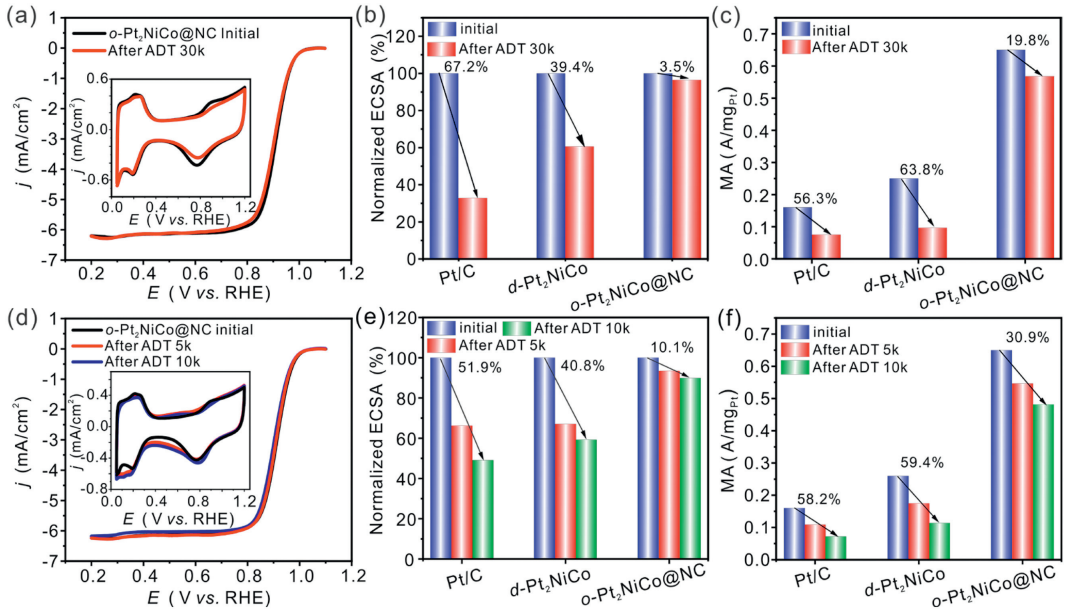

Fig. 4. (a) CV (inset) and LSV curves of *o*-Pt_2NiCo@NC before and after ADT of 30,000 potential cycles between 0.6 V and 1.0 V (*vs.* RHE) in O_2-saturated 0.1 mol/L $HClO_4$. (b) The ECSA and (c) MA comparison of the three catalysts before and after ADT. (d) CV (inset) and LSV curves of *o*-Pt_2NiCo@NC before and after high potential ADT of 5000 and 10,000 potential cycles. (e) The ECSA and (f) MA comparison of the three catalysts before and after high potential ADT.

agglomeration of the Pt_2NiCo particles during high-temperature annealing process, so that more active sites could be exposed on the surface of catalyst. However, when the DCD additive amount continued to increase, the ECSA began to decrease, which indicated that too thick carbon layer would cover the active sites on the surface of the catalyst particles, and even if it could inhibit the agglomeration of the particles, it would still have a negative effect on the ORR performance. In the LSV curves of the samples synthesized with different DCD additions (Fig. S10b in Supporting information), the ORR performance of the catalysts also exhibits a trend of increasing and then decreasing, and reached the optimum at the DCD additions of 0.6 mmol, which was in line with the trend of the CV curves, and it indicated that the thickness of the carbon layer was most suitable at the DCD additions of 0.6 mmol.

Long-term durability is also a critical factor for evaluating the comprehensive performance of catalysts. To evaluate the ORR durability of *o*-Pt_2NiCo@NC, accelerated durability tests (ADT) of 0.6–1.0 V (*vs.* RHE) in O_2-saturated 0.1 mol/L $HClO_4$ was performed. Fig. 4a and Fig. S11 (Supporting information) illustrate the CV and LSV curves of *o*-Pt_2NiCo@NC before and after 30,000 potential cycles. Compared with *d*-Pt_2NiCo and Pt/C (Fig. S12 in Supporting information), the ECSA and half-wave potential attenuation of *o*-Pt_2NiCo@NC is almost negligible. Fig. S13 (Supporting information) further demonstrates the changes of half-wave potentials before and after ADT for the three catalysts, it can be clearly observed that the half-wave potential of *o*-Pt_2NiCo@NC decays by only 8 mV after ADT, which is much lower than that of *d*-Pt_2NiCo (49 mV) and Pt/C (44 mV). The decay ratios of ECSA and MA at 0.9 V (*vs.* RHE) after ADT were further calculated (Figs. 4b and c). The ECSA of *o*-Pt_2NiCo@NC only decays by 3.5% after 30,000 potential cycles, whereas *d*-Pt_2NiCo and Pt/C decayed by 39.4% and 67.2%, respectively. Similarly, the MA at 0.9 V (*vs.* RHE) of *o*-Pt_2NiCo@NC shows a slight degradation of 19.8% relative to *d*-Pt_2NiCo (63.8%) and Pt/C (56.3%). The above analysis of the ADT results fully confirms the excellent long-term durability of *o*-Pt_2NiCo@NC, which is attributed to the protection provided by the N-doped carbon layer confinement, which can effectively inhibit the agglomeration and detachment of the nanoparticles during the catalyst's prolonged operation in acidic electrolyte. Meanwhile, the order intermetallic structure can also mitigate the leaching of transition metals and maximize the preservation of the catalyst's activity. The superior durability exhibited by *o*-Pt_2NiCo@NC is highly competitive among Pt-based ORR electrocatalysts reported in the relative literature recently (Fig. S14 and Table S2 in Supporting information). The superior durability can also be confirmed by the structural characterization of *o*-Pt_2NiCo@NC after ADT. The TEM images of *o*-Pt_2NiCo@NC after 30,000 potential cycles are shown in Fig. S15a (Supporting information). It can be obviously observed that the catalyst nanoparticles are still uniformly dispersed on the carbon support after durability test without obvious agglomeration phenomenon occurs. Moreover, the structure of the carbon layer confinement is still intact without visible damage (Fig. S15b in Supporting information), which also demonstrates that the confinement structure can exhibit excellent durability. Moreover, the Pt 4f high resolution XPS spectrum of *o*-Pt_2NiCo@NC after ADT has nearly no change compared with the initial (Fig. S16 in Supporting information), suggesting a stable electronic structure of Pt.

During the actual start/stop process of PEMFCs, the anode will be exposed to H_2 and O_2 at the same time and forming the H_2-O_2 interface, thus the fuel cell will have a partial reverse current due to the water electrolysis process, which will lead to the decrease of the local potential of the anode and the sudden increase of the cathode voltage [55,56]. Excessive cathodic potentials can be detrimental to the corrosion of the catalyst's carbon carrier and lead to the oxidation of Pt. Therefore, durability testing of the catalyst under harsh operating conditions is equally indispensable [57]. To simulate the catalyst changes in real operating conditions more realistically, high potential ADT tests were performed. During the high potential ADT process, the scanning potential range was increased to 1.0–1.5 V (*vs.* RHE) in O_2 saturated 0.1 mol/L $HClO_4$. Meanwhile, the scanning rate was simultaneously increased to 500 mV/s, and the temperature of the test was increased to 60 °C [58]. The CV and LSV curves of the three catalysts before and after high potential ADT are shown in Fig. 4d and Fig. S17 (Supporting information), respectively. In Fig. S18 (Supporting information), the change in the half-wave potential of the three catalysts after high potential ADT is also intuitively compared. The half-wave potentials of *o*-Pt_2NiCo@NC decayed only 7 mV and 11 mV after 5000

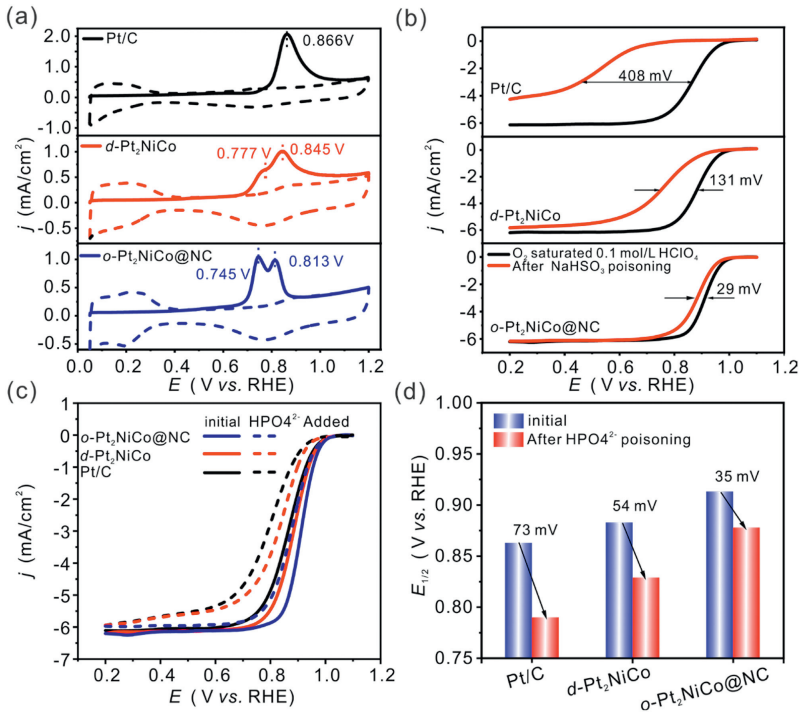

Fig. 5. (a) CO stripping curves of *o*-Pt_2NiCo@NC, *d*-Pt_2NiCo and Pt/C. (b) LSV curves of the three catalysts before and after the existence of 50 mmol/L $NaHSO_3$. (c) LSV curves of the three catalysts before and after the existence of 50 mmol/L Na_2HPO_4 and (d) corresponding change of half-wave potential.

and 10,000 high potential cycles, which were much lower compared with *d*-Pt_2NiCo (18 mV, 39 mV) and Pt/C (15 mV, 34 mV). The decay ratios of ECSA and MA at 0.9 V (*vs.* RHE) after high potential ADT were further calculated (Figs. 4e and f). Among them, the ECSA of *o*-Pt_2NiCo@NC only decayed by 10.1% after 10,000 high potential cycles, while *d*-Pt_2NiCo and Pt/C decayed by 40.8% and 51.9%, respectively. Similar to the trends of ECSA and half-wave potentials, the MA at the 0.9 V (*vs.* RHE) of *o*-Pt_2NiCo@NC decreased by 28.7% after 10,000 high potential cycles, which was significantly lower than the 59.4% of *d*-Pt_2NiCo and the 58.2% of Pt/C. Comprehensive analysis of the results of the above high potential ADT demonstrates that even under severe operating conditions, *o*-Pt_2NiCo@NC can still maintain relatively superior durability due to the carbon layer confinement and the ordered intermetallic structure of internal nanoparticles.

To save the overall cost of PEMFCs, the fuel used for the anode is mainly cheap crude H_2 obtained by steam reforming, but some CO will inevitably be mixed inside [59]. At the same time, the source of cathode O_2 mainly comes from the air, which has a small amount of SO_x due to atmospheric pollution. In addition, some PO_x will also exist in high temperature phosphoric acid doped polymer electrolyte membrane fuel cells. These toxic molecules will poisoning the active sites of Pt and cause the deactivation of the catalysts. Therefore, enhancing the toxicity tolerance of catalysts is also crucial [30,59,60]. The toxicity tolerance of *o*-Pt_2NiCo@NC was also evaluated by CO stripping and LSV technology [54]. The CO stripping curves of the three catalysts are shown in Fig. 5a, in which *o*-Pt_2NiCo@NC exhibit a significantly negatively shifted CO oxidation peak potential, indicating that its surface has the weakest adsorption capacity for CO molecules, confirming its superior CO tolerance. Fig. 5b illustrates the LSV curves of the three catalysts before and after the addition of a certain amount of $NaHSO_3$ to the electrolyte. As expect, *o*-Pt_2NiCo@NC also exhibits superior SO_x tolerance, the half-wave potential of the poisoned ORR only attenuates by 29 mV. In contrast, the half-wave potential decrease of *d*-Pt_2NiCo is 131 mV after SO_x poisoning, and the decrease of Pt/C even reached 408 mV, which almost completely lost the catalytic activity. Fig. 5c shows the LSV curves of the three catalysts before and after the addition of Na_2HPO_4 in the electrolyte. As shown in Fig. 5d, the half-wave potential of *o*-Pt_2NiCo@NC also decays only 35 mV after PO_x poisoning, its PO_x tolerance is also superior to *d*-Pt_2NiCo and Pt/C. According to the results of the above poisoning tests, *o*-Pt_2NiCo@NC also exhibits enhanced tolerance to CO, SO_x and PO_x. The superior toxic tolerance of *o*-Pt_2NiCo@NC may be attributed to the physical protection function provided by the carbon layer, which could isolate the contact between the Pt_2NiCo nanoparticles and toxic molecules to some extent. In addition, the doping of the carbon layer with N elements having stronger electronegativity can help modify the local charge and spin density of carbon, thus inducing the charge transfer and in turn reducing the adsorption between *o*-Pt_2NiCo@NC and toxic molecular [30].

In summary, combining the carbon layer confinement strategy and the ternary Pt-based alloy ordering strategy can effectively facilitate the comprehensive ORR performance. The N-doped carbon layer coated on the Pt_2NiCo intermetallic nanoparticles can not only restrict the particle agglomeration during the high-temperature ordering process, but also mitigate the detachment, corrosion and poisoning of the intermetallic nanoparticles during the long-term operation process. As a result, the *o*-Pt_2NiCo@NC exhibits MA and SA of 4.1 and 5.4 times that of Pt/C, respectively, which demonstrates superior long-term durability in both conventional and high potential cycling tests. Furthermore, *o*-Pt_2NiCo@NC also shows significantly enhanced tolerance to toxic molecules. This approach provides a novel strategy for developing Pt-based ORR catalysts with high activity, long-term durability and toxicity tolerance.

Declaration of competing interest

The authors declare that they have no known competing financial interests or personal relationships that could have appeared to influence the work reported in this paper.

CRediT authorship contribution statement

Chenhao Zhang: Writing – original draft, Methodology, Investigation, Formal analysis, Conceptualization. **Qian Zhang:** Validation. **Yezhou Hu:** Methodology. **Hanyu Hu:** Validation. **Junhao Yang:** Validation. **Chang Yang:** Investigation. **Ye Zhu:** Validation. **Zhengkai Tu:** Validation. **Deli Wang:** Supervision, Resources, Funding acquisition.

Acknowledgments

This work was supported by the National Natural Science Foundation (No. 22279036) and the Innovation and Talent Recruitment Base of New Energy Chemistry and Device (No. B21003). We thank the Analytical and Testing Center of Huazhong University of Science and Technology for allowing us to use its facilities for Raman spectrum measurements.

Supplementary materials

Supplementary material associated with this article can be found, in the online version, at doi:10.1016/j.cclet.2024.110429.

References

[1] Q. Sun, X.H. Li, K.X. Wang, et al., Energy Environ. Sci. 16 (2023) 1838–1869.
[2] M. Song, Q. Zhang, T. Shen, G. Luo, D. Wang, Chin. Chem. Lett. 35 (2024) 109083.
[3] Z. Li, Y. Hu, K. Chen, et al., Acta Phys. Chim. Sin. 37 (2021) 2010029.
[4] H. Zhang, P.K. Shen, Chem. Rev. 112 (2012) 2780–2832.
[5] K. Jiao, J. Xuan, Q. Du, et al., Nature 595 (2021) 361–369.
[6] X. Liu, Z. Zhao, J. Liang, et al., Angew. Chem. Int. Ed. 62 (2023) e202302134.
[7] Y. Jiao, Y. Zheng, M. Jaroniec, S. Qiao, Chem. Soc. Rev. 44 (2015) 2060–2086.
[8] J. Li, W. Xia, X. Xu, et al., J. Am. Chem. Soc. 145 (2023) 27262–27272.
[9] G. Fisseha, Y. Hu, Y. Yu, et al., Chin. Chem. Lett. 35 (2024) 108445.
[10] M. Song, W. Liu, J. Zhang, et al., Adv. Funct. Mater. 33 (2023) 2212087.
[11] B. Genorio, D. Strmcnik, R. Subbaraman, et al., Nat. Mater. 9 (2010) 998–1003.
[12] H.Y. Kim, T. Kwon, Y. Ha, et al., Nano Lett. 20 (2020) 7413–7421.
[13] V.R. Stamenkovic, B.S. Mun, M. Arenz, et al., Nat. Mater. 6 (2007) 241–247.
[14] C. Li, X. Ba, X. Jiang, et al., J. Electrochem. 29 (2023) 2210241.
[15] C. Kim, F. Dionigi, V. Beermann, et al., Adv. Mater. 31 (2019) 1805617.
[16] J. Li, Z. Wei, J. Electrochem. 24 (2018) 589–601.
[17] W. Xiao, W. Lei, M. Gong, H.L. Xin, D. Wang, ACS Catal. 8 (2018) 3237–3256.
[18] W. Yan, X. Wang, M. Liu, et al., Adv. Funct. Mater. 34 (2024) 2310487.
[19] Z. Wang, X. Yao, Y. Kang, et al., Adv. Funct. Mater. 29 (2019) 1902987.
[20] J. Li, Z. Xi, Y.T. Pan, et al., J. Am. Chem. Soc. 140 (2018) 2926–2932.
[21] D. Wang, H.L. Xin, R. Hovden, et al., Nat. Mater. 12 (2013) 81–87.
[22] X. Niu, R.Y. Shao, L. Zhang, et al., Mater. Chem. Front. 7 (2023) 3390–3397.
[23] T.W. Song, M.X. Chen, P. Yin, et al., Small 18 (2022) 2202916.
[24] M. Gong, J. Zhu, M. Liu, et al., Nanoscale 11 (2019) 20301–20306.
[25] X. Ye, R.Y. Shao, P. Yin, H.W. Liang, Y.X. Chen, Inorg. Chem. 61 (2022) 15239–15246.
[26] J. Liang, Z. Zhao, N. Li, et al., Adv. Energy Mater. 10 (2020) 2000179.
[27] L. Bu, N. Zhang, S. Guo, et al., Science 354 (2016) 1410–1414.
[28] J. Qin, P. Zou, R. Zhang, et al., ACS Sustain. Chem. Eng. 10 (2022) 14024–14033.
[29] T.W. Song, C. Xu, Z.T. Sheng, et al., Nat. Commun. 13 (2022) 6521.
[30] T. Najam, S.S.A. Shah, W. Ding, et al., Angew. Chem. Int. Ed. 57 (2018) 15101–15106.
[31] Y. Hu, S. Wang, T. Shen, Y. Zhu, D. Wang, Energy Storage Sci. Technol. 11 (2022) 1264–1277.
[32] X. Bai, S. Yan, J. Wang, et al., J. Mater. Chem. A 2 (2014) 17521–17529.
[33] W.J. Ong, L.L. Tan, Y.H. Ng, S.T. Yong, S.P. Chai, Chem. Rev. 116 (2016) 7159–7329.
[34] H. Jin, Z. Xu, Z.Y. Hu, et al., Nat. Commun. 14 (2023) 1518.
[35] W. Ren, W. Zang, H. Zhang, et al., Carbon 142 (2019) 206–216.
[36] H. Jiang, J. Gu, X. Zheng, et al., Energy Environ. Sci. 12 (2019) 322–333.
[37] C. Hu, L. Dai, Adv. Mater. 29 (2017) 1604942.
[38] H. Kim, K. Lee, S.I. Woo, Y. Jung, Phys. Chem. Chem. Phys. 13 (2011) 17505–17510.
[39] N.P. Subramanian, X. Li, V. Nallathambi, et al., J. Power Sources 188 (2009) 38–44.
[40] F. Lin, F. Lv, Q. Zhang, et al., Adv. Mater. 34 (2022) 2202084.
[41] L. Guo, W.J. Jiang, Y. Zhang, et al., ACS Catal. 5 (2015) 2903–2909.
[42] M. Li, Y. Cai, J. Zhang, et al., Nano Res. 15 (2022) 3230–3238.
[43] Y. Hu, X. Guo, T. Shen, Y. Zhu, D. Wang, ACS Catal. 12 (2022) 5380–5387.
[44] C. Chen, Y. Kang, Z. Huo, et al., Science 343 (2014) 1339–1343.
[45] H. Zhang, P. Shi, X. Ma, et al., Adv. Energy Mater. 13 (2023) 2202703.
[46] Y. Xiong, Y. Yang, F.J. DiSalvo, H.D. Abruña, ACS Nano 14 (2020) 13069–13080.
[47] Y. Li, X.F. Lu, S. Xi, et al., Angew. Chem. Int. Ed. 61 (2022) e202201491.
[48] R. Gui, H. Cheng, M. Wang, et al., Adv. Mater. 36 (2024) 2307661.
[49] K. Wang, H. Yang, Q. Wang, et al., Adv. Energy Mater. 13 (2023) 2204371.
[50] W. Shi, J. Zhang, X. Dong, et al., Carbon 214 (2023) 118321.
[51] Q. Zhang, T. Shen, M. Song, et al., J. Energy Chem. 86 (2023) 158–166.
[52] Y. Ding, W. Zhou, J. Gao, F. Sun, G. Zhao, Adv. Mater. Interfaces 8 (2021) 2002091.
[53] L. Liu, G. Zeng, J. Chen, et al., Nano Energy 49 (2018) 393–402.
[54] Y. Hu, T. Shen, X. Zhao, et al., Appl. Catal. B: Environ. 279 (2020) 119370.
[55] F. Ettingshausen, J. Kleemann, A. Marcu, et al., Fuel Cells 11 (2011) 238–245.
[56] A. Zana, J. Speder, N.E.A. Reeler, T. Vosch, M. Arenz, Electrochim. Acta 114 (2013) 455–461.
[57] Y. Hu, J. Zhang, T. Shen, et al., Small Methods 5 (2021) 2100937.
[58] Z. Qiao, S. Hwang, X. Li, et al., Energy Environ. Sci. 12 (2019) 2830–2841.
[59] X. Wang, Y. Li, Y. Wang, et al., Proc. Natl. Acad. Sci. U. S. A. 118 (2021) e2107332118.
[60] C. Roth, N. Benker, T. Buhrmester, et al., J. Am. Chem. Soc. 127 (2005) 14607–14615.